

An Adaptive Tracking Algorithm for Convection in Simulated and Remote Sensing Data

BHUPENDRA A. RAUT,^a ROBERT JACKSON,^b MARK PICEL,^b SCOTT M. COLLIS,^b MARTIN BERGEMANN,^c AND CHRISTIAN JAKOB^d

^a *Indian Institute of Tropical Meteorology, Ministry of Earth Sciences, Pune, Maharashtra, India*

^b *Environmental Science Division, Argonne National Laboratory, Argonne, Illinois*

^c *ARC Centre of Excellence for Climate Extremes, School of Earth Science, University of Melbourne, Melbourne, Victoria, Australia*

^d *ARC Centre of Excellence for Climate Extremes, School of Earth, Atmosphere and Environment, Monash University, Melbourne, Victoria, Australia*

(Manuscript received 22 May 2020, in final form 21 January 2021)

ABSTRACT: A robust and computationally efficient object tracking algorithm is developed by incorporating various tracking techniques. Physical properties of the objects, such as brightness temperature or reflectivity, are not considered. Therefore, the algorithm is adaptable for tracking convection-like features in simulated data and remotely sensed two-dimensional images. In this algorithm, a first guess of the motion, estimated using the Fourier phase shift, is used to predict the candidates for matching. A disparity score is computed for each target–candidate pair. The disparity also incorporates overlapping criteria in the case of large objects. Then the Hungarian method is applied to identify the best pairs by minimizing the global disparity. The high-disparity pairs are unmatched, and their target and candidate are declared expired and newly initiated objects, respectively. They are tested for merger and split on the basis of their size and overlap with the other objects. The sensitivity of track duration is shown for different disparity and size thresholds. The paper highlights the algorithm's ability to study convective life cycles using radar and simulated data over Darwin, Australia. The algorithm skillfully tracks individual convective cells (a few pixels in size) and large convective systems. The duration of tracks and cell size are found to be lognormally distributed over Darwin. The evolution of size and precipitation types of isolated convective cells is presented in the Lagrangian perspective. This algorithm is part of a vision for a modular platform [viz., TINT is not TITAN (TINT) and Tracking and Object-Based Analysis of Clouds (tobac)] that will evolve into a sustainable choice to analyze atmospheric features.

KEYWORDS: Convective-scale processes; Storm tracks; Algorithms; Cloud tracking/cloud motion winds; Radars/Radar observations; Remote sensing; Satellite observations

1. Introduction

Automated estimation of trajectories of multiple moving objects and analysis of their properties in subsequent images is desired in many industrial and research applications. Several generic object tracking methods have been devised for both real-time and offline tracking (Ristic et al. 2003). However, different objects, recorded by various imaging methods, have complicated characteristics such as nonrigid shapes, fuzzy boundaries, variations in target's size and velocity, uneven illumination, splitting, merging, and occlusion by other objects (Yang et al. 2011; Storlie et al. 2009). Hence, algorithms are better customized for domain-specific tracking using knowledge-based constraints on the estimates of the tracks (Welch and Foxlin 2002).

Automated tracking of thunderstorms and convective clouds in radar and satellite data has been carried out since the 1970s. Most algorithms use area overlap, cross correlation, and centroid shift to associate target objects with the candidates in the subsequent frames. Cross correlations computed using phase shift in the Fourier transforms of images has proven efficient for estimating cloud motion vectors on a fixed grid (Leese et al. 1971). The method is still widely used for deriving

cloud motion vectors from geostationary satellite images (Schmetz et al. 1993; Kishtawal et al. 2009).

In 1974, the National Oceanic and Atmospheric Administration (NOAA) released rainfall analysis and echo tracking software to identify and track rain areas in radar data (Östlund 1974). The software used the centroid and area of the closed contours to match the echoes on a frame-by-frame basis. It was capable of considering splits, mergers, birth, and death of the echoes based on subjective rules. However, the program could not identify multiple splits and mergers and produced erratic tracks for high target density due to a lack of an optimized data association.

Later, Reid (1979) and Crane (1979) presented a more analytical approach for detection and tracking of convection. Reid used Bayesian filtering to map probabilities of objects in the radar frames. This algorithm was immune to cluttered images, false detection, and missing scans. Crane used three-dimensional structural attributes and reflectivity of clusters of the cells to match them from earlier frames using statistical techniques. Tracks produced by both the algorithms were more accurate than NOAA's software due to optimized data association methods and better treatment of birth, death, mergers, and splits of echoes (Östlund 1974). Similar methodologies were used by adding meteorological constraints specific to the tracking problem (Rosenfeld 1987; Arnaud et al. 1992; Dixon and Wiener 1993; Johnson et al. 1998; Limpert et al. 2015).

Corresponding author: Bhupendra Raut, bhupendra.raut@gmail.com

Even today the overlapping method (Moseley et al. 2013), clusters (Lakshmanan et al. 2015), and centroid method (Goswami and Bhandari 2013) are used for tracking cloud systems. Adaptive Kalman filtering (Rossi et al. 2015) and fuzzy logic algorithm (Jung and Lee 2015) have been used for probabilistic tracking in radar data. Machine learning algorithms are also used to track mesoscale convective systems (MCSs) in radar data for the conterminous United States (Haberlie and Ashley 2018).

The Thunderstorm Identification, Tracking, Analysis, and Nowcasting (TITAN) software developed by Dixon and Wiener (1993) is a highly specialized radar tracking software. TITAN identifies thunderstorms using reflectivity thresholds and three-dimensional attributes of the storm. Tracking is achieved by pairing similar storms using combinatorial optimization to find the shortest tracks. Intuitive rules similar to Östlund (1974) are used to reduce ambiguities in storm association and accommodate mergers and splits. The legacy TITAN was improved by treating mergers and split and by correctly estimating the motion using the overlapping method (e.g., Han et al. 2009). However, both TITAN versions suffer due to incorrect “jump” from a decayed cell to a new convection cell and mismatch in case of linear or multicell storms and MCSs (Lakshmanan and Smith 2010).

TITAN is the most popular software among the nowcasting and operational radar communities due to its utilities for weather radar and the source code availability. However, it has a rigid workflow and a highly customized tracking methodology that is only applicable to radar volume reflectivity data. Therefore, tracking of the convective features in two-dimensional radar or satellite images that are preidentified using independent methods (e.g., Steiner et al. 1995; Raut et al. 2008) or simulated data (e.g., Heus and Seifert 2013; Stein et al. 2015) is not feasible with TITAN. Nevertheless, this is a requirement for many research applications. Lately, some tracking codes designed with assumptions about the storm’s physical properties, such as the intensity, coverage, and dBZ thresholds, have been made available (Haberlie and Ashley 2018; Heikenfeld et al. 2019).

The above algorithms perform well in tracking large storms that cover less distance between the radar scans than their size and overlaps in the subsequent frames. However, tracking the high density of individual convective cells (few pixels in size) that do not overlap and are usually short-lived (2–4 scans) is not within the scope of the above methods. Because in such circumstances, a good first guess of the motion is required. Therefore, some recent algorithms have introduced a first guess of the motion from external sources such as forecast wind, manually obtained initial shift, and average motion of other systems (Kyznarová and Novák 2009; Limpert et al. 2015; Heikenfeld et al. 2019). As the first guess drives the later tracking, such algorithms are exposed to errors at this stage (Johnson et al. 1998). Similarly, tracking with an adaptive filter (e.g., Kalman or particle filter method) without first guess requires at least a few steps to improve the gain. On the other hand, the cross-correlations (CC) method efficiently estimates the mean shift in the images using the fast Fourier transform (FFT). However, CC is not used to track the individual objects,

and it may also produce erratic estimates of motion in case of differently moving objects in the frame.

We developed an algorithm for tracking convection by utilizing the strengths of the above tracking methods and minimizing their limitations. For example, the CC method is used for deriving the first guess of the motion, and the Hungarian method is used for combinatorial matching of the objects. The rules in the previously mentioned algorithms inspired treatments of mergers and split events. In addition, we formulated a morphology-based disparity metric that incorporates the change in size, the shift of the objects, and overlapping area. The objects’ meteorological characteristics, such as reflectivity, brightness temperature, or three-dimensional structure of the storms, are not required at any stage. Therefore, the algorithm is useful for tracking various features in a variety of two-dimensional images.

The R language source code for this version of the algorithm is archived on Zenodo (<https://doi.org/10.5281/zenodo.4314194>). The Python version “TINT is not TITAN” (TINT; Picel et al. 2018) is also freely available on GitHub (<https://github.com/openradar/TINT>). A detailed description of the algorithm is presented in section 2 and demonstrations of tracking in radar and simulated data over Darwin, Australia, are presented in sections 3a–3f, followed by a comparison of the TINT and Tracking and Object-Based Analysis of Clouds (tobac) algorithms in section 3g. A short conclusion and an outlook for plans and improvements are presented in section 4.

2. Algorithm

The algorithm works in three stages and is shown in Fig. 1. In the first stage, we estimate the flow using the Fourier phase shift and use this as the first guess to predict the search region for an object in the next frame. In the second stage, we search for potential candidates in the predicted region and compute the disparity score for each pair. These two stages are first implemented for all the objects in the pair of subsequent images. The third stage uses the Hungarian method to find the best matches in the second image for all the objects present in the first image. The expired and the newly initiated objects are also treated at this stage. The following subsections describe the algorithm in detail.

a. Scope and definitions

The algorithm is designed for convection like objects in two-dimensional images. We assume nonrigid objects that can change shape and size; however, they should have well-defined boundaries. The algorithm only works with the bilevel images (i.e., background = 0 and object = nonzero). Instead of occlusion of the objects splitting and merging of the objects is considered.

The identification and tracking are considered two separate operations, and the user is free to use thresholds of reflectivity or more complex methods (e.g., Steiner et al. 1995; Raut et al. 2020) to identify the storm or one can also use the differential reflectivity Z_{DR} /specific differential phase K_{DP} columns to track the most intense convective cores. In the case of simulated data, it is possible to track the regions of updrafts or

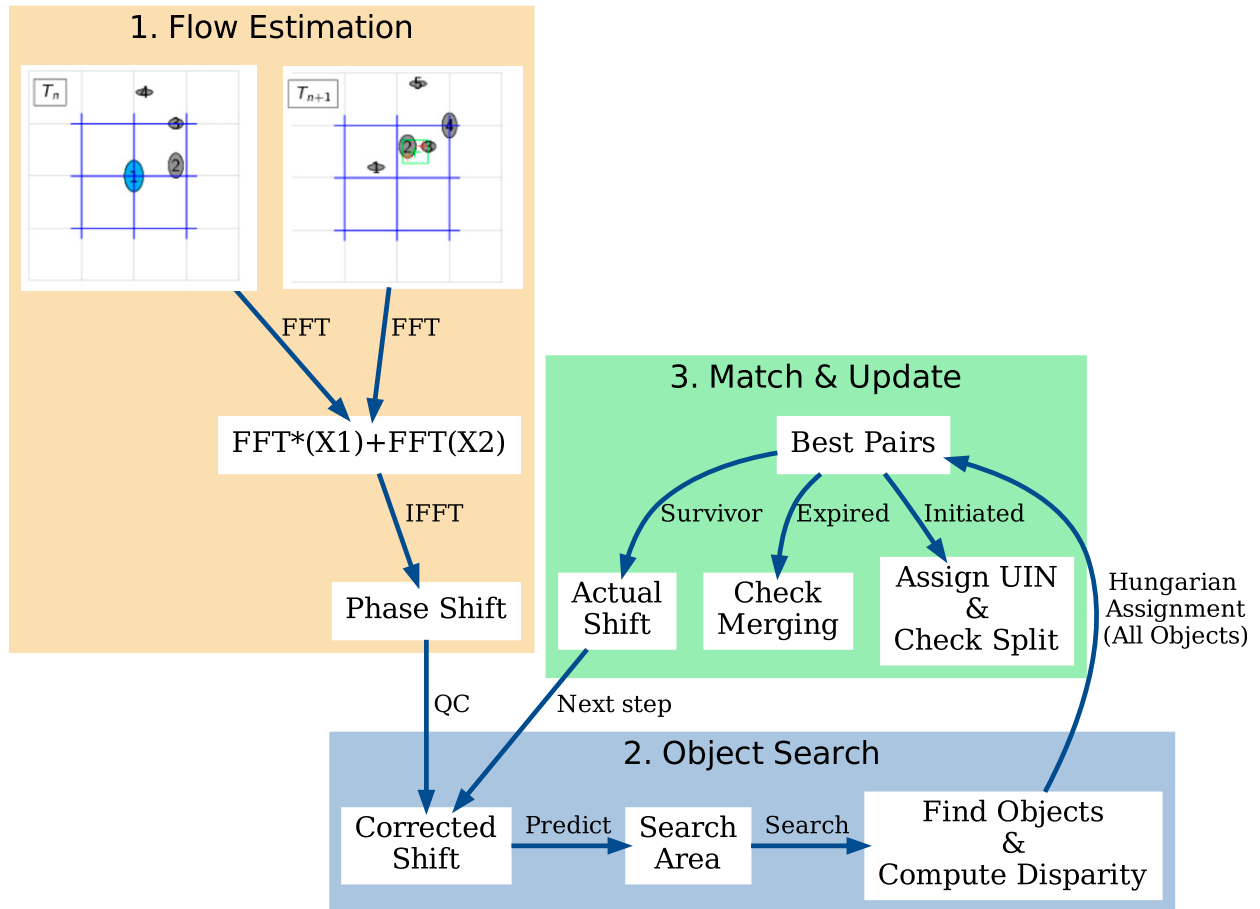


FIG. 1. Schematic of prototype for the integrated nonphysical tracking algorithm that is described in section 2. The first two stages, viz., flow estimation and object search, are performed on all of the objects independently (sections 2b and 2c). Then the Hungarian matching is performed on all objects at once (section 2d). The final step is to check for merge and split events (section 2e). Here, QC = quality control step, FFT^* = the complex conjugate of the FFT, and IFFT = inverse FFT.

heavy rain. The algorithm can also track convective clouds and thunderstorms in satellite images and lows and fronts in reanalysis data.

1) OBJECTS

The input images need to have a clearly defined background (filled with zeros) and the objects (nonzero values). The algorithm tracks all the objects in the image except the objects smaller than the user-defined object size (usually 2–10 pixels). In this study, a contiguous area of at least four nonzero grid points is defined as a single object. The two pixels, diagonally connected by a single point, are not part of the same object. However, two apparently separate objects connected by a single pixel (on the side) are considered a single object. All such objects are labeled with temporary identification numbers in the given image.

2) CENTER OF THE OBJECT

In storm forecasting and analysis, defining the center that aligns with the storm's most intense part is crucial. However, our goal is to accurately identify and label the same storm in

the subsequent images without using the object's physical properties. Hence, we have a choice of the center defined by the geometric mean or median instead of the conventional intensity weighted center. We found that as long as the center lies within the storm, it is applicable for tracking. The center, defined by the geometric mean of irregular shapes, may lie outside the object boundaries. Therefore, we defined medians of indices of all the object's pixels $c(\tilde{x}, \tilde{y})$ as the center if it lies inside the object. If $c(\tilde{x}, \tilde{y})$ happens to fall outside the object boundary, the nearest object pixel is identified as the center. Thus, the center pixel of an object is always part of the object.

The merger and splits are mainly responsible for jumps in the centers defined by the geometric medians. Such jumps also occur for intensity weighted center in rapidly developing multicell storms (e.g., squall line). For example, when the older convective core weakens, the intensity weighted center jumps toward a more intense developing convection in the same storm. The merging and split events will also cause similar jumps in both the type of centers. The current algorithm is robust in handling such scenarios. Although the geometric median is used in tracking, the intensity weighted center can

be stored or computed after the tracking step as per user requirement.

3) ELLIPSE PARAMETERS

The shape of several meteorological features can be approximated by an ellipse. The algebraic ellipse fit method by Fitzgibbon et al. (1999) is applied due to its suitability for irregularly shaped objects. We defined the circularity index (CI) as the ratio of major to minor axes (b/a). The CI computed using the above method gives an approximate idea of the elongation of the objects. We also save other ellipse parameters, including the orientation of the object. Using these parameters, one can classify the storms into the categories linear and circular for further analysis (e.g., Jirak et al. 2003; Nesbitt et al. 2006).

b. Estimation of flow and corrections

An initial estimation of each object's motion is necessary to track them in sequences of images accurately. A fast way to estimate the shift in the object's location in the consecutive images is by computing the phase shift using the FFT (Fig. 1; see the appendix). However, multiple objects moving in different directions is a primary reason for the errors in the CC method. Therefore, as opposed to the gridded approach used by Leese et al. (1971) and the later studies, we estimated flow between the two consecutive time steps within a sufficiently small region (called the "flow region") surrounding the target object. The flow region is a square area with the sides equal to the sum of the object's length (major axis) and a buffer margin. The buffer margin is set equal to the maximum expected speed (explained in the next paragraph). Even if multiple objects occasionally appear in the region, there will be a small chance of scattered motion between them, hence giving precise estimates of the object's motion. Also, with fewer candidates, the data association is done with more certainty.

In the case of rigid objects, the shape, size, and structure do not change in subsequent images; hence, the procedure described in appendix accurately estimates the shift. However, with nonrigid objects, the flow is approximate. The method is likely to overestimate the shift by a considerable magnitude when multiple objects are present in the scene. Therefore, we need to apply quality control measures to truncate the magnitude of the shift. We set the value of the maximum expected speed to 75 km h^{-1} (i.e., approximately 21 m s^{-1}). The user can change this parameter as required. We recommend setting this value on a higher side (say, $>20 \text{ m s}^{-1}$) for better quality control. If the estimated shift is more than the maximum expected shift, then it is truncated. The quality check also utilizes the recorded motion in the previous time step from the second time step onward. At this stage, the initial guess is computed as the mean of the estimated shift and the object's recorded motion in the previous time step, unless any motion component differs by more than the predefined magnitude. In such cases, we use the previous time step as an initial guess assuming that phase shift failed to capture the motion. This stage ensures that the algorithm gets a reliable estimate of the motion in various situations.

A search region is predicted using the corrected shift, and the objects that are partially or entirely in the region are identified as candidates. The small size of the search region for smaller objects significantly reduces the number of objects in the

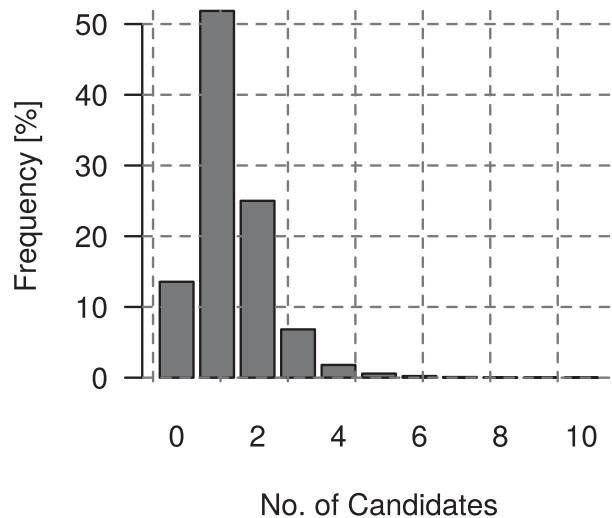


FIG. 2. A frequency histogram of the number of candidate objects found in the search region for 209 296 target objects over Darwin during the 2016/17 wet season.

scene. In Darwin radar data, approximately 90% of the targets had two or fewer candidates in the search region (see Fig. 2). Of these, approximately 13.5% targets had no candidates, and approximately 52% and 25% targets have one and two candidates, respectively. Less than 1% of the targets had five or more candidates. This step largely reduces the burden on the assignment stage (section 3d). Moreover, the search region's radius is proportional to the object's equivalent diameter; hence, only large objects tend to have numerous (>5) candidates. However, the overlapping criterion skillfully handles such cases.

c. The cost function of disparity

For each candidate–target pair a cost function of disparity D is computed as follows:

$$D = d_c + d_p + \sqrt{a_c} - \sqrt{a_o}, \quad (1)$$

where d_c is the distance of the center of the candidate from the center of the target, and d_p is that from the predicted location. a_c is the difference in the target and the candidate object's areas, and a_o is the overlap area for the pair.

We take the square root of the quantities with area units (km^2) to maintain the units of distance for all the terms in the disparity function. Thus, the area terms become comparable to the distance terms, and their complete dominance on the cost function is avoided. Also, a small change in the size of a large object will not have an excessive contribution to the disparity. A disparity matrix is obtained for all the pairs, at time step T_m , by repeating stages 1 and 2 in Fig. 1. The best match for each target object is decided using the method described in section 3d.

The cost function [Eq. (1)] works well with the first three terms in most situations except for considerably large objects. An example is a mesoscale convective system covering an extensive area in the radar coverage. Such objects are slow moving and, given their size, may have significant overlapping areas from one image to the next. However, they may also

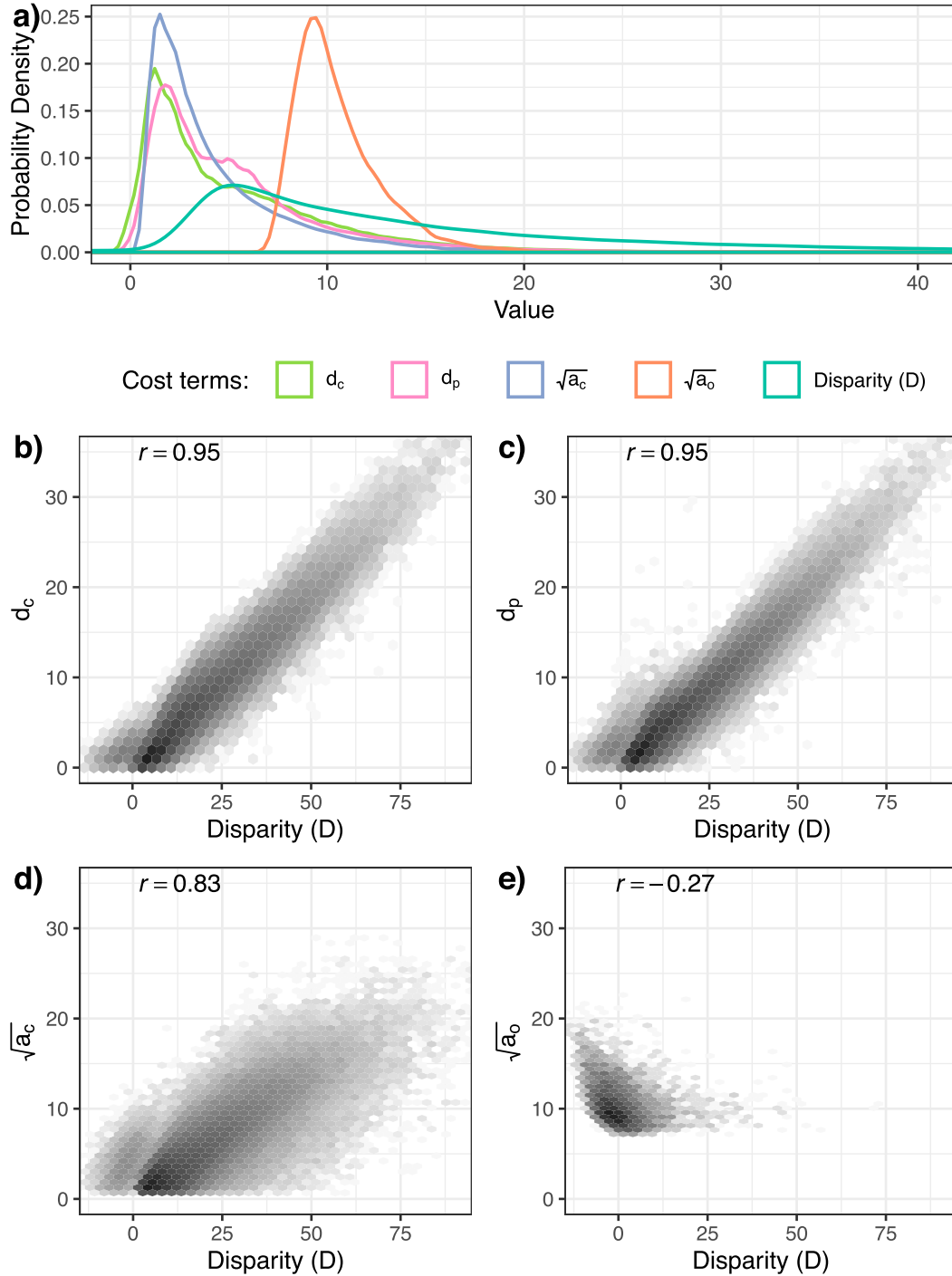


FIG. 3. (a) Probability density of the values of disparity and its four disparity terms [Eq. (1)] for all of the potential pairs of the objects. (b)–(e) Relation of disparity and the four disparity terms.

undergo a significant change in shape and size, causing large shifts in the object's center. Shifts in the center can also occur due to multiple merging or splitting events for large objects. Such events considerably increase the disparity of the larger objects owing to the first three terms. For such objects, the disparity will shoot up to the maximum allowed disparity for

pairing. Therefore, the square root of the overlapping area is added as a negative cost term to handle large objects. This fourth term of the cost function is only computed for the objects larger than the specified size.

It is essential to understand the interrelation of disparity terms to fix the maximum acceptable disparity between the

matched objects. In Fig. 3a, we show the kernel probability density functions of the four cost function terms and the disparity in Eq. (1) for all the potential target–candidate pairs from radar images during the 2016/17 wet season over Darwin. The first three terms of the disparity have comparable distributions. The overlapping term is zero in the case of small objects but significant for large objects.

Figures 3b–e show scatterplots and correlations of the four disparity terms against the total disparity. The distance terms, d_c and d_p , are strongly correlated with each other ($r = 0.91$, not shown) and with the disparity (for both $r = 0.95$). The correlation coefficients of the area terms $\sqrt{a_c}$ and $\sqrt{a_o}$ with disparity are 0.83 and -0.27 , respectively. The correlation coefficients of both the distance terms with the area term $\sqrt{a_c}$ are approximately 0.7. However, their correlations with the area term $\sqrt{a_o}$ are not significant. Moreover, the area terms $\sqrt{a_c}$ and $\sqrt{a_o}$ are weakly correlated to each other ($r = 0.13$). Hence, the area overlap term $\sqrt{a_o}$ is the most independent parameter that influences the disparity. The overlapping criterion applied to approximately 2.5% of the total potential pairs when objects larger than 625 km^2 are checked for overlapping. For approximately 58% of these pairs, the disparity was zero or less. Thus, the overlapping criterion plays a dominant and important role in matching large objects.

d. The Hungarian assignment

The disparity matrix for all the objects, obtained in section 3c, serves as the basis of matching the best pairs. The optimal one-to-one assignment between the sets of objects in two images is solved using the Hungarian method (Kuhn 1955; Hornik 2005). The method does not neglect any object and only takes nonnegative values of disparity. Therefore, the negative values of disparity are set to zero. The Hungarian method works on an $m \times m$ disparity matrix (say, \mathbf{x}); hence, we add dummy objects to the matrix when the number of objects in both images are unequal. For a given disparity matrix \mathbf{x} , the method iteratively finds a permutation p of the numbers from 1 to m such that the global disparity

$$G = \sum_{i=1}^m \mathbf{x}[i, p(i)] \quad (2)$$

is minimized. Each target object at T_n is assigned to precisely one candidate at T_{n+1} such that the total disparity for best matches is minimized.

Because the Hungarian method matches every object to exactly one object, some undesirable pairs with significant disparity exist. Therefore, the pairs with more than a predetermined disparity ($D_{\max} = 45 \text{ km}$ for this study) are unpaired, and the corresponding target objects are labeled as expired, and the candidate objects are labeled as initiated objects. Similarly, objects assigned to dummy candidates (target) are also labeled as initiated (expired). Each target is given a unique integer identity number (UIN) at the time of its birth. When a new object is initiated, the next available UIN is assigned to it.

e. Splits and mergers

Merging or splitting is defined as a joining or separation of two or more convective objects (Westcott 1984; Dixon and

Wiener 1993). Convective cells often merge into or split from a larger convective structure. If the region between the two objects gets filled for a short time in radar/satellite data, the objects will appear to have merged and then split in subsequent time steps, causing the “jump” error due to multiple merging and splitting (Lakshmanan and Smith 2010). Two nearby objects get attached during the merge events, and the resulting object at least partially overlaps with both the merging objects area in the previous image (Zan et al. 2019). Similarly, during the split events, a single object breaks into two or more objects, and the resulting objects partially overlap the region of the original object. We confirmed it by visual inspection of the radar and satellite images.

The split or merge begins as detachment or attachment of the two nearby convective regions due to the dissipating or growing connecting region. Therefore, the overlapping criterion works very well for determining if the merge and split happened. We check the possibility of splitting and merging when the newly initiated or expired objects are recorded after the Hungarian matching. Note that the merge and split events are sensitive to the segmentation method or reflectivity thresholds and the observations’ time interval.

In this algorithm, a new object is considered an offspring if an existing object of comparable size was found in the overlapping region before its birth. When a split occurs, a resulting object with the least disparity to its parent will carry the parents UIN, and the new object will be called offspring with a next available UIN. An offspring can only have a single parent object, but there can be multiple offspring of the same parent object.

Similarly, if a surviving object at T_n overlaps with an expired object at T_{n-1} , then the expired object is considered to have merged in the surviving object. The joint object should live until at least one time step later than the expired objects. If such a merge event occurs, the resulting object carries the earlier UIN. In other words, the algorithm considers the merging of smaller objects into a larger object like the end of the smaller object. The UIN of the larger object in which the smaller object is merged is stored. Several objects are allowed to merge into a single object. The genealogy of an object can be generated using the saved parameters.

3. Applications and results

Section 3 demonstrates convection tracking in radar and simulated data over Darwin using the above method. Section 3g compares the track statistics with the tobacco method in NEXRAD data over Houston.

a. The CPOL radar data

We demonstrate the algorithm’s utility by tracking the convective cells in CPOL radar data over Darwin (-12.245°N , 131.045°E), for the 2016/17 wet season (from 12 October 2016 to 2 May 2017). C-band polarimetric (CPOL) radar is a dual-polarization Doppler radar working at a 5.6-GHz frequency with a 10-min horizontal scan interval. The data were calibrated using Louf et al. (2019b) and gridded to a Cartesian grid of $2.5 \text{ km} \times 2.5 \text{ km} \times 0.5 \text{ km}$ resolution with 40 vertical levels

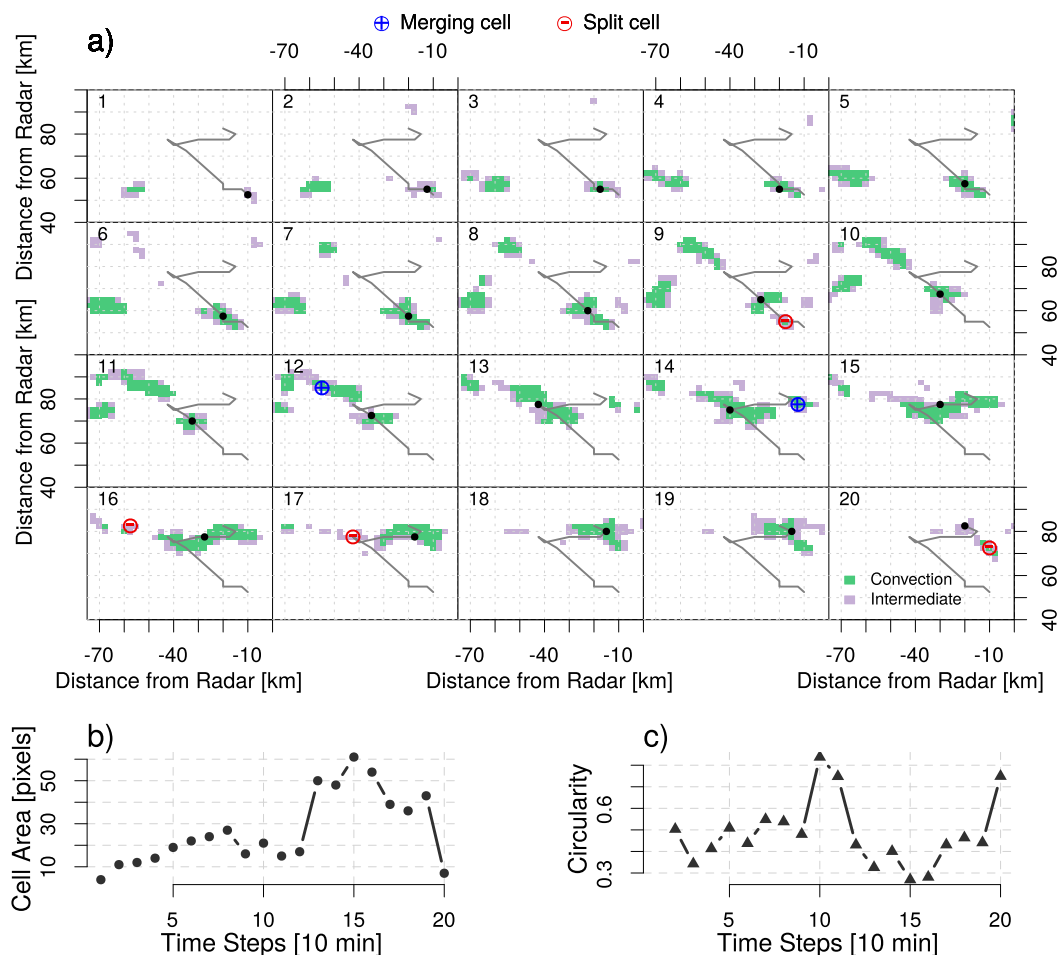


FIG. 4. The life cycle of a convective cell was observed near Darwin from 0420 to 0730 UTC 11 Mar 2017. (a) The track and center of the convective cell are projected over the input images. The encircled plus and minus symbols show the cells before the merge and after the split events involving the target cell, respectively. Convective and intermediate echo classifications are adopted from Raut et al. (2020). Also shown are the (b) area and (c) circularity index of the target cell during its lifetime.

from 0.5 to 20 km of altitude. The corrected reflectivities at the 3-km level are used for separating convective and intermediate pixels using the wavelet-based method of Raut et al. (2020). In this classification, convective pixels tend to be associated with strong updrafts, and the intermediate pixels represent the regions of a weaker updraft or dying convection. Usually, storms tend to be dominated by intermediate type during the initiation and the dissipation stages. The resulting 10-min-resolution images with convective and intermediate regions are given as input to the algorithm. However, because of the algorithm's bilevel nature, all of the pixels of the same object will have the same label; hence, the tracking will not be affected by the object's convective and intermediate classification.

b. A single track analysis

We first show the tracking of a convective storm observed over the Tiwi Islands in Darwin on 11 March 2017 (Fig. 4). The

storm survived for more than three hours (0420–0730 UTC) and encountered two merge and four split events. Figure 4a is focused on the tracked system, and each panel shows convective and intermediate regions at the respective time step. Note that the intermediate type of Raut et al. (2020) is associated with moderate updrafts and the convective type is associated with strong updrafts. The cell initiated with all intermediate pixels but quickly developed a larger convective region. The full estimated track and the merge and the split events are projected over the radar images. The evolution of the echo size and circularity is shown in Figs. 4b and 4c. The CI reduced as the system increased in the size due to the merging at time steps 13 and 15. The algorithm tracked the convective cell during its growth (from 4 to 50 pixels) and decay by successfully handling the changes in size and direction. It also accurately detects the merge and split events. As expected, every merge and split event is associated with the increasing and decreasing size of the cell. The convection area and CI are good indicators of

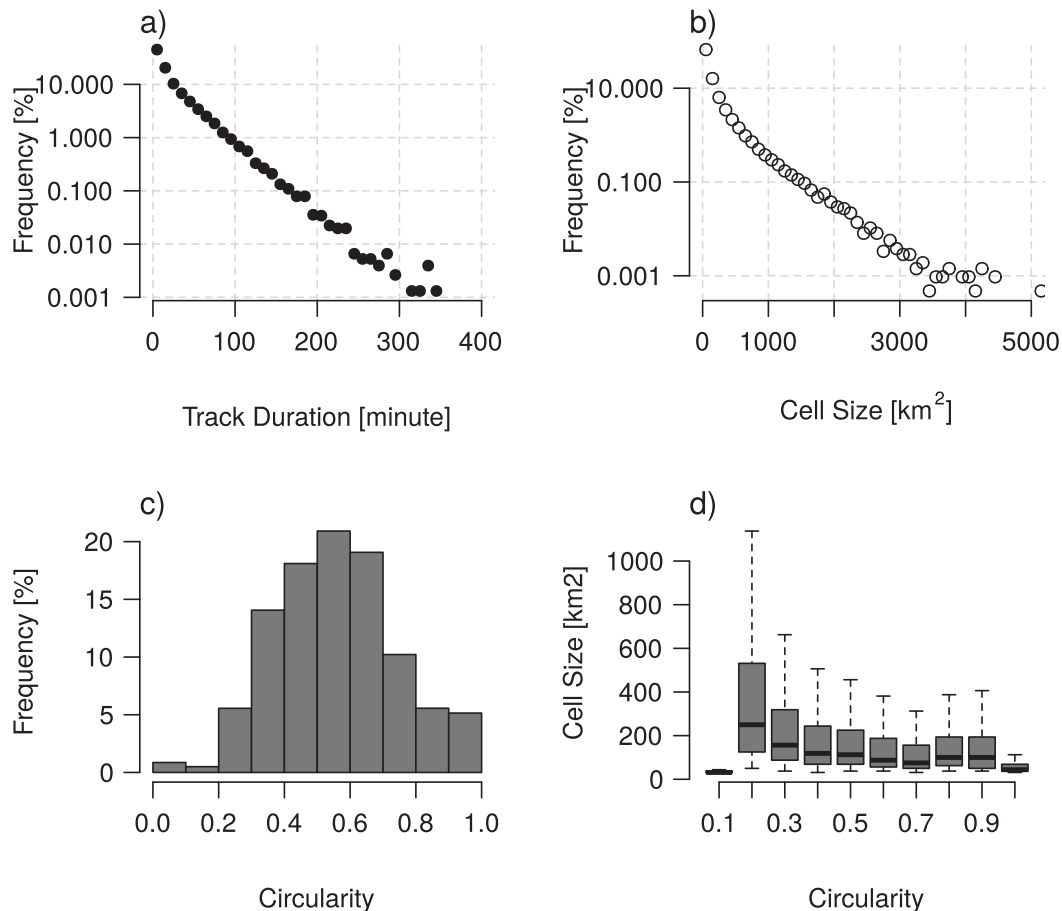


FIG. 5. Frequency histograms of (a) duration of tracks, (b) area, and (c) CI of the convective region, along with a (d) box-and-whiskers plot for size of the convective regions for CI for Darwin during the 2016/17 wet season.

shape (linear or circular) and spread of the convective region throughout the track duration.

c. Size, duration, and shape statistics

The algorithm estimated 75 987 tracks in 28 425 radar scans for the 2016/17 wet season. The algorithm detected that approximately 40% of the echoes initiated by splitting, and approximately 16% of the echoes merged into other convective echoes. The frequency histogram of the track duration at 10-min bin size and recorded cell sizes at 100-km² bin size, shown in Figs. 5a and 5b, respectively, are lognormally distributed. A large number of convective cells are of small size and short duration. Large cells are infrequent and are likely to have a longer duration. Similar results are noted by earlier studies over tropical Australia (May and Ballinger 2007; Peter et al. 2015; Louf et al. 2019a). Over the Darwin region, the convective rain rate is a strong function of cell area, and large cells are associated with the most intense rainfall due to localized convection (Louf et al. 2019a). The long-duration tracks (duration > 300 min) are usually associated with large cell sizes and several mergers throughout the life cycle.

The CI is normally distributed (Fig. 5c) with a mean and median equal to approximately 0.55. A small number of echoes (10%) are more or less circular, and fewer echoes (2%) are

linear. The median area of linear echoes, with CI = 0.2, is larger (250 km²) than that of circular echoes with CI = 0.9 (100 km²; Fig. 5d). The mean CI and the mean and the maximum size of the convective cell during its lifetime have a weak but significant negative correlation ($r = -0.15$ and $r = -0.16$, respectively). The above results agree with our expectations that the larger continuous convective regions (usually multicell systems) tend to organize in lines (Houze 2014). The track duration also has a weak but significant correlation with the maximum cell size ($r = 0.12$). The correlation of track duration with mean cell size and CI are not significant.

d. Life cycle of convective storms

Tracking methods are required to study convective storms from a Lagrangian perspective by following the storm growth and decay rather than collecting statistics at fixed times. To demonstrate this, the most independent long-lived tracks were selected with the following criteria, and changes in their size and convective and intermediate fractions are studied. The isolated convective storms with a long life cycle are selected using the following criteria:

- 1) Self-generation: should not be a product of splitting.
- 2) Isolated dissipation: should not merge at the expiry.

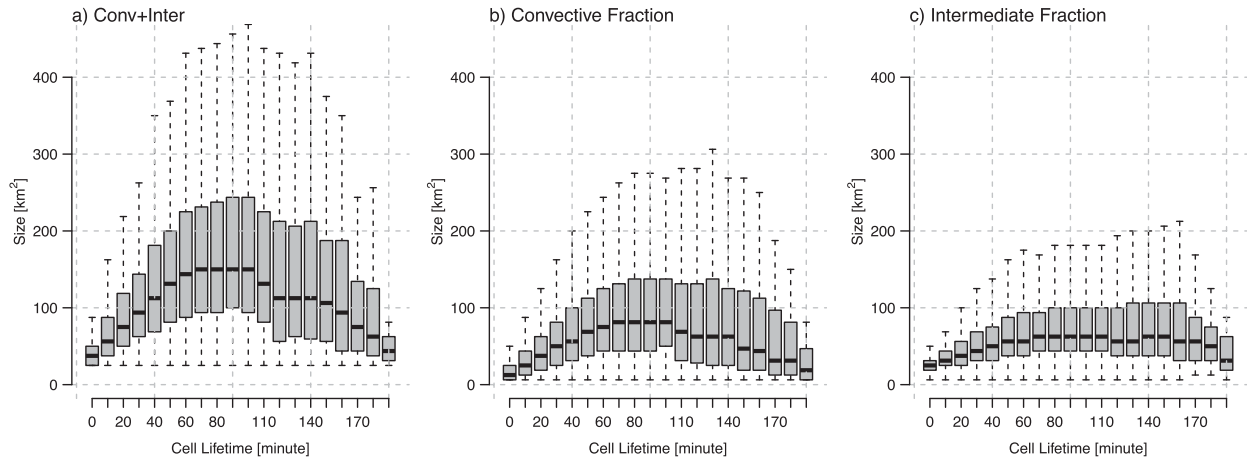


FIG. 6. Variation of (a) storm size, (b) fraction of convective type, and (c) fraction of intermediate type during the lifetime of 524 selected tracks over Darwin during the 2016/17 wet season. See section 3d for the selection criterion.

- 3) Unconnected: no other cell is split from or merged into the cell.
- 4) Long duration: lifetime between 120 and 200 min.
- 5) Attain a maximum size of $>100 \text{ km}^2$.
- 6) Remained inside the radar domain.

We found 524 isolated convective storms following the above criteria. Figure 6 shows the total area change and the fraction of convective and intermediate types as the storms evolved. Although the individual tracks in this example may have evolved in various pathways, the plots show the general trend in the development of such storms. In general, the isolated storms grow and attain their maximum size in the first one hour when the storm size increased due to an increase in both convective and intermediate types. Kyznarová and Novák (2009) plotted the mean size of the storm using dBZ thresholds for different track durations and found similar growth for more prolonged duration storms. In their matured phase, the convective and intermediate fraction is maintained. However, in the dissipation phase, storm size reduces due to the reduced convective area while the intermediate area is maintained. 29% storms had all intermediate pixels in their first observed time step, whereas 47% storms had all intermediate pixels in their final time step. Only 4% of the storms had all intermediate pixels in one of the time step during their matured phase. Thus, the matured phase of the convective storms is dominated by the strong updraft region and the weaker updraft can be seen at the time of genesis and dissipation.

e. Sensitivity analysis

As stated in section 2d, after the combinatorial matching the pairs with large disparity (D_{\max}) are unpaired. The corresponding target objects are considered expired, and candidate objects are considered initiated objects. The tracks of the large objects are also affected by invoking overlap criteria. Sensitivity to these thresholds can sometimes have severe implications for the accuracy of the tracks. Therefore, histograms of track duration for wide range of values of D_{\max} are plotted in Fig. 7a. The shorter tracks are not affected by the D_{\max} threshold. However, the frequency of longer tracks is directly

proportional to D_{\max} . The doubling of D_{\max} from 30 to 60 km increases the frequency of a 100-min duration tracks from 0.5% to 1%. The threshold for the objects' size for invoking overlap criteria has no effect on the track duration except for the longer tracks (Fig. 7b). Note that less than 2% of the pairs used this criterion, and it has a significant impact on the tracks of large objects that are important but less frequent. Therefore, inclusion of the overlapping criterion is crucial.

f. Application to model data

This subsection demonstrates the algorithm's application to investigate the storm life cycle and the statistics of extreme rainfall events in the simulated data. The tracking algorithm is applied to subkilometer simulations within the limited-area version of the Met Office Unified Model (UM) during 11–19 November 2006 over the Tiwi Islands (11.6°S , 130.9°E), roughly 80 km north of Darwin. The model was run to create an ensemble of 8 members at two different resolutions (1.33 and 0.44 km). Storm tracks with intensities in the fifth quintile, in an ensemble simulation of extreme convective events, are shown in Fig. 8. Colored tracks represent different ensemble members. First, the rain-rate threshold of 0.1 mm h^{-1} was used to separate raining areas of a minimum storm size of 2 pixels. We tracked all the continuous regions identified by the above criteria, regardless of their intensity or duration. Therefore, the smaller rainfall areas are also included in the tracking, some of which become intense storms. We separated the storms of interest for further analysis from all the tracks. Most storms propagated from east to west, and they are initiated and dissipated over the center of the islands. The subkilometer simulations produced more storms of shorter duration than the 1.33-km simulations. A similar comparison of the simulated storm tracks with the observed storm tracks can reveal the differences in the diurnal cycle and sources of rainfall bias in the simulations.

g. Comparison with tobac

This section assesses the performance of the algorithm's Python version (TINT) in tracking convection against the tobac algorithm (Heikenfeld et al. 2019). Tobac first determines

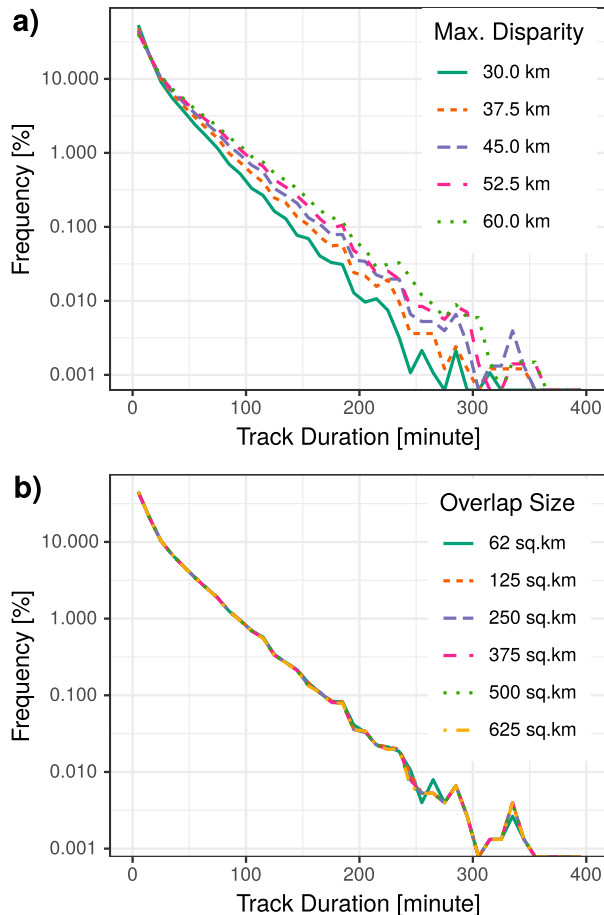


FIG. 7. Sensitivity of duration of tracks shown by the frequency histograms for various thresholds of (a) maximum disparity acceptable between the paired objects and (b) minimum size of the object to invoke overlap criterion.

the objects present in the images through user-specified thresholds then tracks the features by searching the next image within a search radius determined by a maximum feasible velocity v_{\max} .

The dataset used for comparison is the composite reflectivity from the NEXRAD KHGX radar in the Houston–Galveston,

Texas, area from 1800 to 2000 UTC 30 May 2015. During this time, isolated convective cells were produced due to sea-breeze convergence moving to the west-northwest over the Houston–Galveston area. Both the algorithms were given echoes with composite reflectivity greater than 32 dBZ as input. Tobac erodes features by a set number of pixels to potentially isolate larger interconnected features and to remove spurious small features [refer to [Gonzalez and Woods \(1992\)](#) for erosion operator]. However, TINT removes the objects smaller than the given thresholds (set to 4). Therefore, a pixel erosion threshold of tobac was set to 3 to match the TINT's minimum size criterion so that both algorithms only track features with at least 4 pixels present. However, because of the erosion operator's peculiarity, both algorithms select a slightly different set of objects to track. Therefore, we adjusted the erosion threshold in tobac to ensure that the TINT and tobac are tracking the same objects. For tobac, v_{\max} was set to 10 m s^{-1} following [Heikenfeld et al. \(2019\)](#).

Figure 9 shows that both the algorithms successfully tracked the isolated convection (2, 4, and 6) present just south of Galveston. However, there is a slight difference in the direction and duration of each track (Figs. 9a,b). For example, cells 1 and 3 are tracked by TINT but not by tobac. The erosion in tobac may have removed it. Besides, track 5 in Fig. 9b appears to be different cells being assigned to the same track, as shown by an anomalous shift in direction and velocity. Also, in Fig. 9c, tobac has a bimodal distribution and more tracks longer than an hour compared to TINT. It may be due to an object disappearing while another is present within the assumed search radius, causing fewer but longer tracks in tobac than in TINT (Fig. 9c). The TINT algorithm's disparity function and check for D_{\max} is designed to filter out such events demonstrating an advantage of TINT over tobac. The comparison shows that, given these uncertainties and differences in methodologies, TINT produces tracks within reasonable agreement with those from tobac.

4. Conclusions and future plans

Atmospheric scientists have used several tracking methods to analyze meteorological systems in a Lagrangian frame of reference. Usually, these methods are based on different

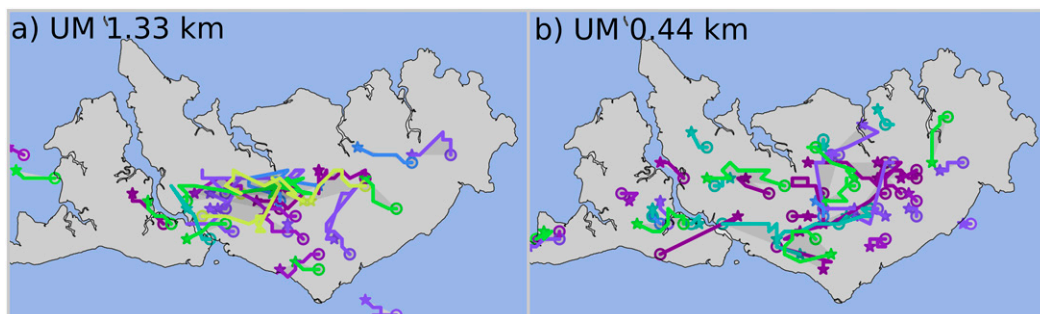


FIG. 8. The tracks of the thunderstorms simulated by the limited-area version of the UM over the Tiwi Islands at (a) 1.33- and (b) 0.44-km horizontal grid resolution. The colors of the lines represent different ensemble members. Here we only showed tracks of the most intense storms in each ensemble. The starting points of the storm tracks are shown by open circles, and their endpoints are shown by stars.

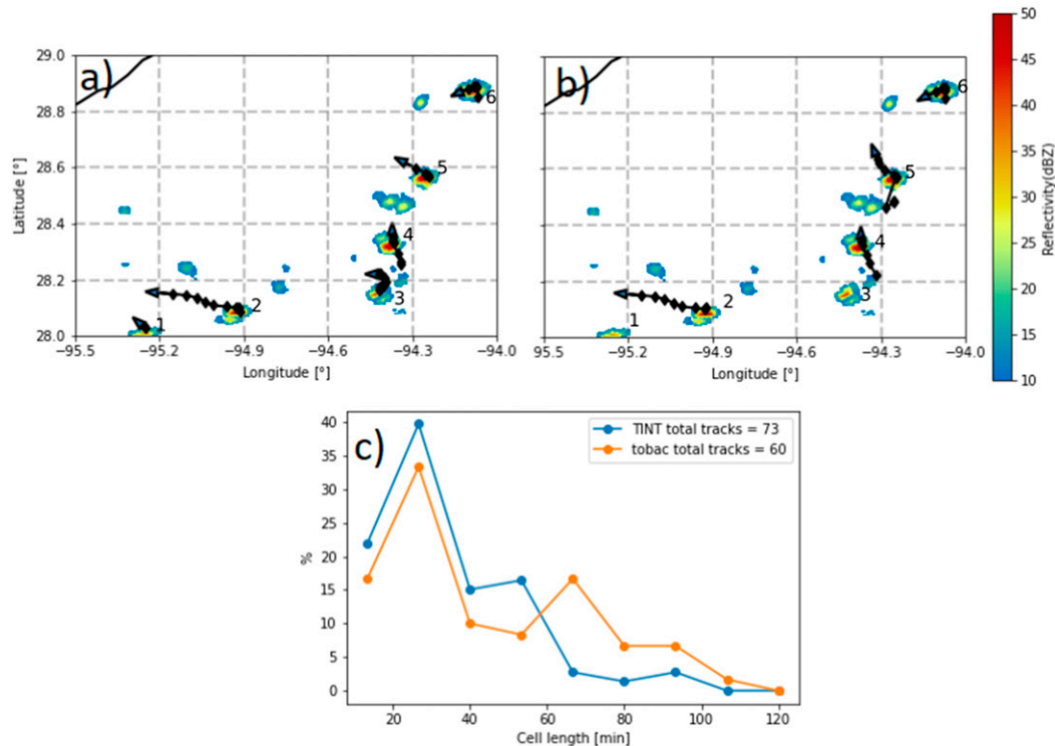


FIG. 9. Composite reflectivity from the NEXRAD KHGX radar at 1900 UTC 30 May 2015 with tracks generated by (a) TINT and (b) tobac overlaid. (c) Normalized frequency histogram of cell lifetime for each cell tracked by TINT and tobac sampled by the KHGX radar at 1800–2000 UTC 30 May 2015.

physical principles and are designed for a specific purpose. Efforts have been made to study the evolution of convection by following individual cells (Rosenfeld 1987; Arnaud et al. 1992; Hu et al. 2019). Many tracking methods are reinvented and coded in contemporary programming languages by several researchers. TITAN fulfills the need for tracking applications for the operational radar community; however, tracking needs for general two-dimensional data are not addressed. Due to the lack of reliable and convenient tracking methods (for discussion, see section 1), the standard practice is to infer the life cycle of convective clouds in simulations and observations using time or domain averaged properties (the Eulerian construct). However, the advances in polarimetric radars, cloud-resolving simulations, and the coverage of the geostationary satellites justify studying the statistical properties of convection in the Lagrangian construct (e.g., the evolution of K_{DP}/Z_{DR} columns, transition probabilities of modes of convection Biello et al. 2010; Kumar et al. 2014).

In this paper, we presented a general-purpose method without making assumptions about the storm's physical properties. This extendable algorithm is designed to work in real-time, offline tracking of convective features in various datasets. The basic algorithm works with bilevel images with background and labeled objects and considers convection-like behavior such as merging and splitting (see section 2a). We demonstrated the capability of the algorithm to track objects in two-dimensional data. Over Darwin, the maximum storm size increases the survival probability, and the larger storms tend to be organized in

more elongated shapes. The storm size and the track duration have lognormal distributions; however, CI is normally distributed. The increasing fraction of active convection characterizes the growth of the storms. As opposed to that, the dissipation is characterized by the increased intermediate fraction and the reduction in convective fraction. Therefore, the storms are bigger and more intense (more convective area than intermediate) during their mature stage. Splitting is found to be more common than the merging of convective storms.

As the algorithm does not consider any physical characteristics of the object, it is flexible for tracking any objects using morphological characteristics, that is, size change, overlapping, and shift in the centers. We converged ideas from several existing methods and designed an integrated tracking system easily applicable for general-purpose tracking by adjusting user-specified parameters. It is a fast and extendable algorithm that aims at meteorological researchers for tracking a variety of features in observed and simulated two-dimensional data. Due to the functional programming approach, it is easily modifiable by advanced users to add newer capabilities. Since developing the algorithm and releasing it as a community codebase, the authors became aware of several efforts to track and analyze atmospheric phenomena. A particularly successful codebase is the tobac tracking framework (Heikenfeld et al. 2019). Truly successful community code needs a critical mass of users, contributors, and maintainers and a diverse funding base. To this end, the TINT development team decided to bring TINT into tobac and join the tobac development team. Our vision is

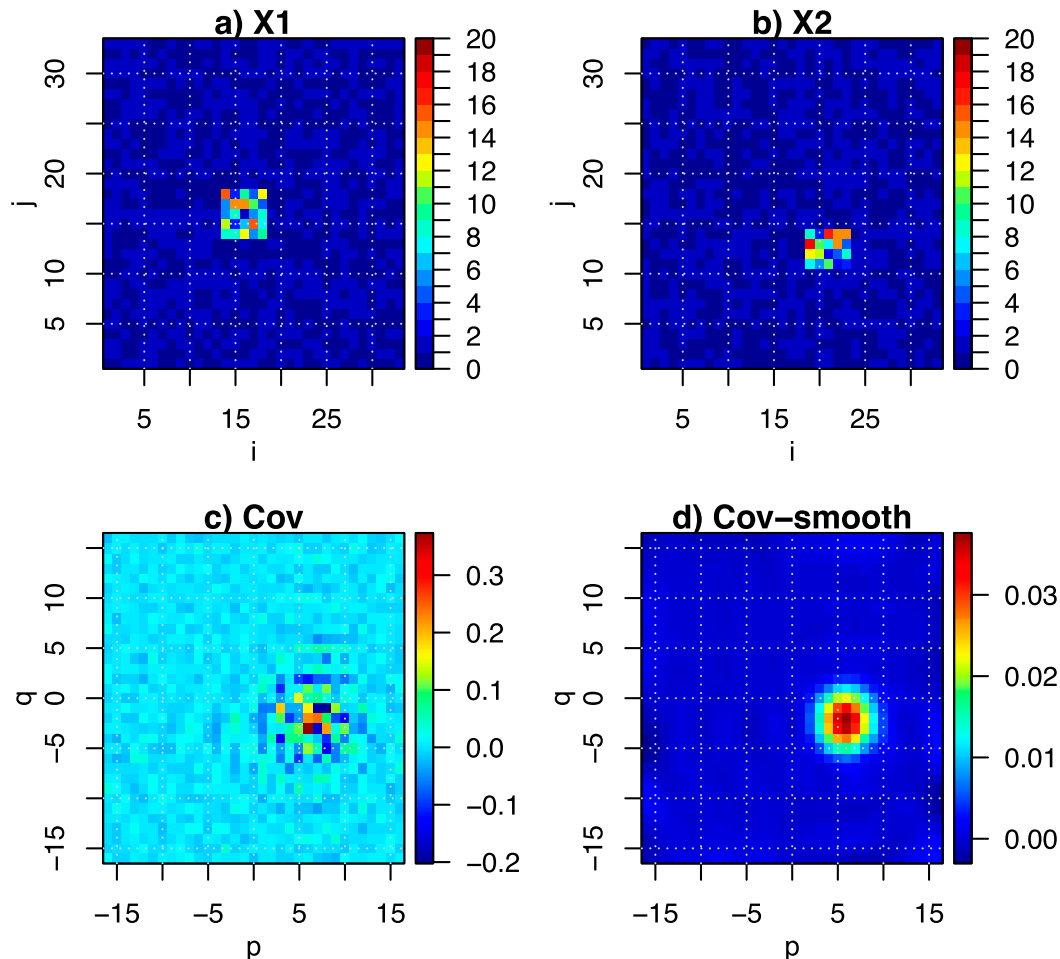


FIG. A1. Estimation of the shift in the object's location in the pair of noisy images. In this example, the actual shift in the center is (5, -3) pixels and the estimated shift is (6, -2) pixels.

that tobac will serve as a modular platform for performing a range of Lagrangian analyses and evolve into a sustainable choice for tracking and analyzing atmospheric features. Contributions from the community are welcome.

Acknowledgments. Development of the algorithm was funded through the Australian Research Council's Center of Excellence for Climate System Science at Monash University. The U.S. Department of Energy Atmospheric Systems Research (ASR) supported the work under Grant DE-SC0014063, "The vertical structure of convective mass-flux derived from modern radar systems—Data analysis in support of cumulus parameterization." The U.S. Department of Energy, Office of Science, Office of Biological and Environmental Research supported the contributions of Scott Collis and Robert Jackson through Argonne National Laboratory, under Contract DE-AC02-06CH11357. Michael Rezný and the late Benjamin Möbis provided valuable suggestions during the development of the prototype algorithm. Valentin Louf and Alan Protat at the Australian Bureau of Meteorology are acknowledged for providing the radar data. The four anonymous reviewers are acknowledged for providing

valuable suggestions, which significantly improved the paper. We appreciate the work of the editorial staff during the COVID-19 pandemic.

Data availability statement. CPOL radar data for Darwin can be obtained from the Atmospheric Radiation Measurement (ARM) data center (<https://www.arm.gov/data/data-sources/cpol-150>). Source code of the method is available on open-access repository (<https://doi.org/10.5281/zenodo.4314194>). The combined source code for TINT and tobac can be found at GitHub (<https://github.com/climate-processes/tobac>).

APPENDIX

The FFT and Cross Correlation

The appendix demonstrates the FFT method to compute the cross-covariance matrix and estimate the shift in the object's location in the pair of images using the method described in [Leese et al. \(1971\)](#). The shift is estimated using the following

procedure. Let $X_1(i, j)$ be an image, centered over the targets object's location at time T_1 and $X_2(i, j)$ be the same region at time T_2 .

- 1) Compute FFT of both of the images $X_1(i, j)$ and $X_2(i, j)$ to obtain $X_1(\mu, \nu)$ and $X_2(\mu, \nu)$.
- 2) Compute $C(\mu, \nu) = X_1^*(\mu, \nu) \cdot X_2(\mu, \nu)$ (the asterisk indicates complex conjugate).
- 3) Perform an inverse FFT on $C(\mu, \nu)/|C(\mu, \nu)|$; the real part of the outcome gives covariance matrix $\text{Cov}(p, q)$.
- 4) Remove noise using Gaussian smoothing on $\text{Cov}(p, q)$.

We generated two dummy images (33×33 pixels) with random background noise and an object with an irregular structure to demonstrate the FFT phase shift's application to estimate the shift (Fig. A1). The object's center is shifted by $(5, -3)$ pixels in the second image, and its shape and size both have changed. The raw covariance matrix $\text{Cov}(p, q)$ results from step 3. Gaussian smoothing is performed ($\sigma = 2$) to remove the high-frequency noise. Note that the sum of the covariance in Figures A1c and A1d is preserved after the smoothing. The location of the maximum covariance in step 4 gives the shift in the images. The shift estimated from the smooth cross-covariance matrix is $(6, -2)$ pixels. Thus, the CC method estimates shifts in the object's location and can be efficiently computed for individual objects using the FFT method.

REFERENCES

- Arnaud, Y., M. Desbois, and J. Maizi, 1992: Automatic tracking and characterization of African convective systems on Meteosat pictures. *J. Appl. Meteor.*, **31**, 443–453, [https://doi.org/10.1175/1520-0450\(1992\)031<0443:ATACOA>2.0.CO;2](https://doi.org/10.1175/1520-0450(1992)031<0443:ATACOA>2.0.CO;2).
- Biello, J., B. Khouider, and A. J. Majda, 2010: A stochastic multicloud model for tropical convection. *Commun. Math. Sci.*, **8**, 187–216, <https://doi.org/10.4310/CMS.2010.v8.n1.a10>.
- Crane, R. K., 1979: Automatic cell detection and tracking. *IEEE Trans. Geosci. Electron.*, **17**, 250–262, <https://doi.org/10.1109/TGE.1979.294654>.
- Dixon, M., and G. Wiener, 1993: TITAN: Thunderstorm Identification, Tracking, Analysis, and Nowcasting—A radar-based methodology. *J. Atmos. Oceanic Technol.*, **10**, 785–797, [https://doi.org/10.1175/1520-0426\(1993\)010<0785:TITTA>2.0.CO;2](https://doi.org/10.1175/1520-0426(1993)010<0785:TITTA>2.0.CO;2).
- Fitzgibbon, A., M. Pilu, and R. B. Fisher, 1999: Direct least square fitting of ellipses. *IEEE Trans. Pattern Anal. Mach. Intell.*, **21**, 476–480, <https://doi.org/10.1109/34.765658>.
- Gonzalez, R. C., and R. E. Woods, 1992: *Digital Image Processing*. 2nd ed. Prentice Hall, 716 pp.
- Goswami, B., and G. Bhandari, 2013: Convective cloud detection and tracking from series of infrared images. *J. Indian Soc.*, 291–299, <https://doi.org/10.1007/s12524-012-0234-3>.
- Haberlie, A. M., and W. S. Ashley, 2018: A method for identifying midlatitude mesoscale convective systems in radar mosaics. Part II: Tracking. *J. Appl. Meteor. Climatol.*, **57**, 1599–1621, <https://doi.org/10.1175/JAMC-D-17-0294.1>.
- Han, L., S. Fu, L. Zhao, Y. Zheng, H. Wang, and Y. Lin, 2009: 3D convective storm identification, tracking, and forecasting—An enhanced TITAN algorithm. *J. Atmos. Oceanic Technol.*, **26**, 719–732, <https://doi.org/10.1175/2008JTECHA1084.1>.
- Heikenfeld, M., P. J. Marinescu, M. Christensen, D. Watson-Parris, F. Senf, S. C. van den Heever, and P. Stier, 2019: tobac 1.2: Towards a flexible framework for tracking and analysis of clouds in diverse datasets. *Geosci. Model Dev.*, **12**, 4551–4570, <https://doi.org/10.5194/gmd-12-4551-2019>.
- Heus, T., and A. Seifert, 2013: Automated tracking of shallow cumulus clouds in large domain, long duration large eddy simulations. *Geosci. Model Dev.*, **6**, 1261–1273, <https://doi.org/10.5194/gmd-6-1261-2013>.
- Hornik, K., 2005: A clue for cluster ensembles. *J. Stat. Software*, **14** (12), 1–25, <https://doi.org/10.18637/jss.v014.i12>.
- Houze, R. A., 2014: *Cloud Dynamics*. Academic Press, 432 pp.
- Hu, J., and Coauthors, 2019: Tracking and characterization of convective cells through their maturation into stratiform storm elements using polarimetric radar and lightning detection. *Atmos. Res.*, **226**, 192–207, <https://doi.org/10.1016/j.atmosres.2019.04.015>.
- Jirak, I. L., W. R. Cotton, and R. L. McAnelly, 2003: Satellite and radar survey of mesoscale convective system development. *Mon. Wea. Rev.*, **131**, 2428–2449, [https://doi.org/10.1175/1520-0493\(2003\)131<2428:SARSOM>2.0.CO;2](https://doi.org/10.1175/1520-0493(2003)131<2428:SARSOM>2.0.CO;2).
- Johnson, J., P. L. MacKeen, A. Witt, E. D. W. Mitchell, G. J. Stumpf, M. D. Eilts, and K. W. Thomas, 1998: The storm cell identification and tracking algorithm: An enhanced WSR-88D algorithm. *Wea. Forecasting*, **13**, 263–276, [https://doi.org/10.1175/1520-0434\(1998\)013<0263:TSCIAT>2.0.CO;2](https://doi.org/10.1175/1520-0434(1998)013<0263:TSCIAT>2.0.CO;2).
- Jung, S.-H., and G. Lee, 2015: Radar-based cell tracking with fuzzy logic approach. *Meteor. Appl.*, **22**, 716–730, <https://doi.org/10.1002/met.1509>.
- Kishtawal, C., S. Deb, P. Pal, and P. Joshi, 2009: Estimation of atmospheric motion vectors from *Kalpana-1* imagers. *J. Appl. Meteor. Climatol.*, **48**, 2410–2421, <https://doi.org/10.1175/2009JAMC2159.1>.
- Kuhn, H. W., 1955: The Hungarian method for the assignment problem. *Nav. Res. Logist.*, **2**, 83–97, <https://doi.org/10.1002/nav.3800020109>.
- Kumar, V. V., A. Protat, C. Jakob, and P. T. May, 2014: On the atmospheric regulation of the growth of moderate to deep cumulonimbus in a tropical environment. *J. Atmos. Sci.*, **71**, 1105–1120, <https://doi.org/10.1175/JAS-D-13-0231.1>.
- Kyznarová, H., and P. Novák, 2009: CELLTRACK—Convective cell tracking algorithm and its use for deriving life cycle characteristics. *Atmos. Res.*, **93**, 317–327, <https://doi.org/10.1016/j.atmosres.2008.09.019>.
- Lakshmanan, V., and T. Smith, 2010: An objective method of evaluating and devising storm-tracking algorithms. *Wea. Forecasting*, **25**, 701–709, <https://doi.org/10.1175/2009WAF2222330.1>.
- , B. Herzog, and D. Kingfield, 2015: A method for extracting postevent storm tracks. *J. Appl. Meteor. Climatol.*, **54**, 451–462, <https://doi.org/10.1175/JAMC-D-14-0132.1>.
- Leese, J. A., C. S. Novak, and B. B. Clark, 1971: An automated technique for obtaining cloud motion from geosynchronous satellite data using cross correlation. *J. Appl. Meteor.*, **10**, 118–132, [https://doi.org/10.1175/1520-0450\(1971\)010<0118:AATFOC>2.0.CO;2](https://doi.org/10.1175/1520-0450(1971)010<0118:AATFOC>2.0.CO;2).
- Limpert, G., A. Houston, and N. Lock, 2015: The advanced algorithm for tracking objects (AALTO). *Meteor. Appl.*, **22**, 694–704, <https://doi.org/10.1002/met.1501>.
- Louf, V., C. Jakob, A. Protat, M. Bergemann, and S. Narsey, 2019a: The relationship of cloud number and size with their large-scale environment in deep tropical convection. *Geophys. Res. Lett.*, **46**, 9203–9212, <https://doi.org/10.1029/2019GL083964>.
- , A. Protat, R. A. Warren, S. M. Collis, D. B. Wolff, S. Raunyar, C. Jakob, and W. A. Petersen, 2019b: An integrated approach to weather radar calibration and monitoring

- using ground clutter and satellite comparisons. *J. Atmos. Oceanic Technol.*, **36**, 17–39, <https://doi.org/10.1175/JTECH-D-18-0007.1>.
- May, P. T., and A. Ballinger, 2007: The statistical characteristics of convective cells in a monsoon regime (Darwin, northern Australia). *Mon. Wea. Rev.*, **135**, 82–92, <https://doi.org/10.1175/MWR3273.1>.
- Moseley, C., P. Berg, and J. O. Haerter, 2013: Probing the precipitation life cycle by iterative rain cell tracking. *J. Geophys. Res. Atmos.*, **118**, 13 361–13 370, <https://doi.org/10.1002/2013JD020868>.
- Nesbitt, S. W., R. Cifelli, and S. A. Rutledge, 2006: Storm morphology and rainfall characteristics of TRMM precipitation features. *Mon. Wea. Rev.*, **134**, 2702–2721, <https://doi.org/10.1175/MWR3200.1>.
- Östlund, S. S., 1974: Computer software for rainfall analyses and echo tracking of digitized radar data. NOAA Tech. Memo. ERL WMPO-15, 82 pp., <https://repository.library.noaa.gov/view/noaa/11233/>.
- Peter, J. R., M. J. Manton, R. J. Potts, P. T. May, S. M. Collis, and L. Wilson, 2015: Radar-derived statistics of convective storms in southeast Queensland. *J. Appl. Meteor. Climatol.*, **54**, 1985–2008, <https://doi.org/10.1175/JAMC-D-13-0347.1>.
- Picel, M., S. Collis, B. Raut, S. Carani, R. Jackson, M. van Lier-Walqui, and A. Fridlind, 2018: TINT—TINT is not TITAN. Easy-to-use tracking code based on TITAN—Details and uses. *Eighth Symp. on Advances in Modeling and Analysis Using Python*, Austin, TX, Amer. Meteor. Soc., 3.4, <https://ams.confex.com/ams/98Annual/webprogram/Paper335460.html>.
- Raut, B. A., R. N. Karekar, and D. M. Puranik, 2008: Wavelet-based technique to extract convective clouds from infrared satellite images. *IEEE Geosci. Remote Sens. Lett.*, **5**, 328–330, <https://doi.org/10.1109/LGRS.2008.916072>.
- , V. Louf, K. Gayatri, P. Murugavel, M. Konwar, and T. Prabhakaran, 2020: A multiresolution technique for the classification of precipitation echoes in radar data. *IEEE Trans. Geosci. Remote Sens.*, **58**, 5409–5415, <https://doi.org/10.1109/TGRS.2020.2965649>.
- Reid, D. B., 1979: An algorithm for tracking multiple targets. *IEEE Trans. Automat. Contr.*, **24**, 843–854, <https://doi.org/10.1109/TAC.1979.1102177>.
- Ristic, B., S. Arulampalam, and N. Gordon, 2003: *Beyond the Kalman Filter: Particle Filters for Tracking Applications*. Artech House, 328 pp.
- Rosenfeld, D., 1987: Objective method for analysis and tracking of convective cells as seen by radar. *J. Atmos. Oceanic Technol.*, **4**, 422–434, [https://doi.org/10.1175/1520-0426\(1987\)004<0422:OMFAAT>2.0.CO;2](https://doi.org/10.1175/1520-0426(1987)004<0422:OMFAAT>2.0.CO;2).
- Rossi, P. J., V. Chandrasekar, V. Hasu, and D. Moiseev, 2015: Kalman filtering-based probabilistic nowcasting of object-oriented tracked convective storms. *J. Atmos. Oceanic Technol.*, **32**, 461–477, <https://doi.org/10.1175/JTECH-D-14-00184.1>.
- Schmetz, J., K. Holmlund, J. Hoffman, B. Strauss, B. Mason, V. Gaertner, A. Koch, and L. Van De Berg, 1993: Operational cloud-motion winds from Meteosat infrared images. *J. Appl. Meteor.*, **32**, 1206–1225, [https://doi.org/10.1175/1520-0450\(1993\)032<1206:OCMWFM>2.0.CO;2](https://doi.org/10.1175/1520-0450(1993)032<1206:OCMWFM>2.0.CO;2).
- Stein, T. H., R. J. Hogan, P. A. Clark, C. E. Halliwell, K. E. Hanley, H. W. Lean, J. C. Nicol, and R. S. Plant, 2015: The DYMECS project: A statistical approach for the evaluation of convective storms in high-resolution NWP models. *Bull. Amer. Meteor. Soc.*, **96**, 939–951, <https://doi.org/10.1175/BAMS-D-13-00279.1>.
- Steiner, M., R. A. Houze Jr., and S. E. Yuter, 1995: Climatological characterization of three-dimensional storm structure from operational radar and rain gauge data. *J. Appl. Meteor.*, **34**, 1978–2007, [https://doi.org/10.1175/1520-0450\(1995\)034<1978:CCOTDS>2.0.CO;2](https://doi.org/10.1175/1520-0450(1995)034<1978:CCOTDS>2.0.CO;2).
- Storlie, C. B., T. C. Lee, J. Hannig, and D. Nychka, 2009: Tracking of multiple merging and splitting targets: A statistical perspective. *Stat. Sin.*, **19**, 1–52.
- Welch, G., and E. Foxlin, 2002: Motion tracking: No silver bullet, but a respectable arsenal. *IEEE Comput. Graph. Appl.*, **22**, 24–38, <https://doi.org/10.1109/MCG.2002.1046626>.
- Westcott, N., 1984: A historical perspective on cloud mergers. *Bull. Amer. Meteor. Soc.*, **65**, 219–226, [https://doi.org/10.1175/1520-0477\(1984\)065<0219:AHPOCM>2.0.CO;2](https://doi.org/10.1175/1520-0477(1984)065<0219:AHPOCM>2.0.CO;2).
- Yang, H., L. Shao, F. Zheng, L. Wang, and Z. Song, 2011: Recent advances and trends in visual tracking: A review. *Neurocomputing*, **74**, 3823–3831, <https://doi.org/10.1016/j.neucom.2011.07.024>.
- Zan, B., Y. Yu, J. Li, G. Zhao, T. Zhang, and J. Ge, 2019: Solving the storm split-merge problem—A combined storm identification, tracking algorithm. *Atmos. Res.*, **218**, 335–346, <https://doi.org/10.1016/j.atmosres.2018.12.007>.